Metrol. Meas. Syst., Vol. 32 (2025) No. 2, pp. 1–18
DOI: 10.24425/mms.2025.154334

PAN POLSKA AKADEMIA NAUK

METROLOGY AND MEASUREMENT SYSTEMS

Index 330930, ISSN 0860-8229
www.metrology.wat.edu.pl

M&MS

A TWO-STAGE ADAPTIVE IDENTIFICATION FRAMEWORK OF THE TIRE ROAD FRICTION COEFFICIENT CONSIDERING THE EFFECT OF MULTIPLE UNKNOWN MEASUREMENT NOISES

Fengjiao Zhang[1)], Bo Zhang[1)], Lanchun Zhang[2)], Ting Meng[3)], Yan Wang[4)]

1) Changzhou Vocational Institute of Mechatronic Technology, College of Transportation Engineering, 26 Mingxin Middle Road, 213164 Changzhou, China
2) Jiangsu University of Technology, School of Automotive and Traffic Engineering, 1801 Zhongwu Road, 213001 Changzhou, China
3) The Hong Kong Polytechnic University, School of Electrical and Electronic Engineering, 11 Kowloon Hung Hom Yuk Choi Road, 999077 Hong Kong, China
4) The Hong Kong Polytechnic University, The Department of Industrial and Systems Engineering, 11 Kowloon Hung Hom Yuk Choi Road, 999077 Hong Kong, China (✉ *yanjack.wang@polyu.edu.hk*)

Abstract

The *tire-road friction coefficient* (TRFC) directly determines the available traction and braking forces of the tires, which in turn has a significant impact on vehicle stability control, particularly for commercial vehicles such as heavy-duty trucks. However, onboard sensors typically cannot directly measure the exact TRFC. To obtain an accurate TRFC, estimation algorithms are used, which rely on data from onboard sensors combined with vehicle and tire models. Since the signals required for estimation come from various types of sensors, in practice accurately obtaining the noise statistical characteristics of all sensors is highly challenging. Additionally, due to the complex and variable nature of vehicle operating conditions, noise tends to be time-varying as a result of environmental factors, which inevitably affects the accuracy of the estimation. To address these problems, we propose a two-stage adaptive identification framework that combines the *extended H-infinity Kalman filter* (EHKF) with the *adaptive unscented Kalman filter* (AUKF). First, in situations where the noise statistical characteristics are unknown, EHKF and the tire model are used to accurately estimate forces on the front and rear axles. Second, considering the time-varying nature of the noise, the AUKF, along with the vehicle model and axial force information, is employed to estimate the TRFC for the front and rear wheels. Finally, simulation tests on various road surfaces demonstrate that the two-stage adaptive identification method outperforms the unscented Kalman filter in terms of accuracy and stability.

Keywords: Tire-road friction coefficient estimation, adaptive identification framework, extended H-infinity Kalman filter, adaptive unscented Kalman filter.

1. Introduction

Rollover accidents have become a frequent road safety concern for commercial vehicles, particularly heavy trucks. Compared to passenger cars, the increased size and weight of heavy vehicles result in a higher risk of rollovers [1–3]. Many experts and scholars have researched rollover prevention, and the timing of the intervention of rollover control strategies is closely

Article history: received November 14, 2024; revised January 10, 2025; accepted February 12, 2025; available online April 10, 2025.

related to the *tire-road friction coefficient* (TRFC). In addition to avoiding accidents through rollover control, it is also possible to reduce the incidence of accidents by controlling steering and braking [4]. Such control systems are often called active collision avoidance systems [5]. A collision avoidance system generally includes motion prediction and path planning [6, 7]. Fully utilizing the TRFC when generating and tracking the path can enhance the system's performance. Furthermore, it is heavy trucks that typically undertake long-distance freight transportation, which inevitably involves different road surfaces, such as asphalt, gravel, or icy roads. On different road surfaces, even the same heavily loaded vehicle has a varying stability margin, making it necessary to identify the TRFC in real-time. In addition, changes in the driving environment, such as road surface conditions, weather, and traffic, can significantly affect measurement noise in vehicle dynamics. For instance, rough or uneven road surfaces introduce high-frequency vibrations, increasing noise in sensor readings such as acceleration or wheel speed. Similarly, environmental factors like rain or snow can alter friction characteristics, leading to greater uncertainty and variability in measurements.

Unfortunately, the TRFC cannot be directly measured using onboard sensors [8]. As a result, it must be estimated through indirect methods. The TRFC is typically estimated using two main approaches: experimental methods and model-based methods [9]. In experiments, optical sensors are attached to the vehicle to collect TRFC-related data, such as tire noise and carcass deformation. The TRFC is then estimated on the basis of the correlation between these measured parameters and the TRFC. Additionally, a position-sensitive detector was used to indirectly measure the real-time deformation of the tire carcass relative to the rim to estimate the TRFC [10]. Other types of sensors, such as piezoelectric sensors, estimated the TRFC by detecting tread deformation [11]. In addition, measuring the TRFC based on accelerometer data is also an effective method [12, 13]. However, these experimental approaches often require the installation of additional sensors, which leads to high costs and limited practicality. Recently, computer vision has been used to estimate the TRFC by analysing road images with machine learning [14, 15]. Machine learning-based methods for identifying the TRFC offer the advantage of adapting to complex, nonlinear relationships between vehicle dynamics and road conditions thus improving prediction accuracy. These methods can also handle large datasets and identify patterns that traditional models may miss. However, their main drawback lies in the need for extensive training data and the risk of overfitting, which may limit their generalizability to unseen road conditions.

Model-based methods typically use standard onboard sensors to acquire signals related to the TRFC and combine them with vehicle dynamics and tire models to estimate the TRFC. Specifically, these approaches can be classified into two main types: ones that rely on longitudinal dynamics and others that focus on lateral dynamics [16, 17]. The methods based on longitudinal dynamics primarily estimate the TRFC using the slip ratio. For example, Lee *et al.* [18] developed a traction estimator that integrates slip curves to estimate the TRFC. Cui *et al.* [19] identified the TRFC based on fitted curves that relate the TRFC to slip ratios under five different road conditions. Additionally, Sharifzadeh *et al.* [20] employed recursive least squares to estimate the TRFC using slip signals. Zhao *et al.* [21] proposed a linear extended state observer to estimate the TRFC based on the braking dynamics model of a two-wheeled vehicle. To enhance estimation accuracy further, many researchers have utilized Kalman filters for TRFC estimation. The *extended Kalman filter* (EKF) has also been applied for TRFC identification [22]. Similar TRFC identification methods have also been documented in the literature [23, 24]. The use of Kalman filtering techniques allows researchers to continuously update their estimates as new data is collected. This real-time processing is particularly beneficial in dynamic driving situations where road conditions may change rapidly. The EKF further refines this process by accommodating non-linearities in the system, providing even more accurate TRFC estimates.

During turning manoeuvres, Hu *et al.* [25] designed an EKF on the basis of vehicle lateral dynamics to estimate the TRFC. To further enhance the identification performance of the TRFC, *unscented Kalman filters* (UKF) have also been employed [26]. For instance, Wang *et al.* [27] introduced a comprehensive estimation scheme based on the UKF to predict the TRFC under conditions of mass mismatch. Additionally, an improved UKF was utilized to address the issue of TRFC estimation in scenarios where data loss occurs [28]. These filters use vehicle nonlinearities for reliable TRFC estimates, especially in cornering. The integration of UKF allows for a more accurate identification of the TRFC by effectively handling uncertainties and variations in the input data.

Recently, as deep learning algorithms have advanced, data-driven approaches have been increasingly used for TRFC estimation. McBride *et al.* [29] compared observer-based methods with neural network-based approaches and found that neural networks operated more quickly and directly while providing accuracy comparable to traditional methods. Xu *et al.* [30] further demonstrated that neural networks could successfully predict tire forces, highlighting the potential of neural network approaches in estimating tire-road interaction dynamics. Furthermore, Sadeghi *et al.* [31] utilized four key features and developed a multilayer neural network to estimate the TRFC. Additionally, a spatial-temporal convolutional neural network was proposed to predict the TRFC with enhanced accuracy [32]. Although data-driven methods have been shown to effectively estimate the TRFC, there still remain significant challenges in terms of data collection and interpretability.

From the above analysis, it is evident that model-based estimation methods remain the dominant approach in current research. These methods typically estimate the TRFC by first determining the tire forces. Estimating tire forces requires data from multiple sensors, such as wheel speed and steering angle signals, while TRFC estimation also relies on vehicle acceleration data. However, the noise characteristics of these sensors are often unknown or time-varying. Existing research rarely takes into account both the influence of unknown noise during tire force estimation and the impact of time-varying measurement noise on the accuracy of TRFC identification. To address these issues, an estimation scheme that integrates the *extended H-infinity Kalman filter* (EHKF) with the *adaptive unscented Kalman filter* (AUKF) has been proposed for TRFC identification. First, considering that the estimation of tire forces is influenced by unknown noise, the EHKF is employed to estimate the longitudinal and lateral forces acting on the tire. It should be noted that due to the use of the single-track model, we assume that the forces on the front axle and rear axle are respectively equal to the sum of the forces on the two front wheels and the two rear wheels. Furthermore, to address the time-varying characteristics of noise during vehicle operation, the AUKF is utilized to achieve real-time estimation of the TRFC with the vehicle model and tire force information. Finally, the two-stage adaptive identification method is validated under various conditions using a co-simulation platform based on *TruckSim* and *MATLAB/Simulink*. Some contributions are listed as follows.

1. A novel estimation method for tire forces is proposed which integrates a tire model with the EHKF. This approach accounts for the influence of completely unknown noise characteristics, enabling precise and robust calculation of tire forces under varying operational conditions.

2. A two-stage adaptive estimation scheme is developed to identify the TRFC. This framework simultaneously addresses noise uncertainties in all input signals associated with the tire and vehicle models, ensuring reliable performance even in the presence of dynamic and unpredictable environmental and system variations.

The remainder of this paper is organized as follows: Section 2 presents the methodology, Section 3 details the simulation tests, and Section 4 provides the conclusions of this study.

2. Methodology

The framework of the two-stage adaptive TRFC estimation is shown in Fig. 1. Initially, the longitudinal and lateral tire forces, along with noise, are estimated using data from onboard sensors and a tire model. Next, these values are input into the EHKF for filtering to obtain more accurate tire forces. Because the vehicle model is a single-track one, the tire forces are aggregated and translated into forces acting on the front and rear axles. Then, using the vehicle model and AUKF, the TRFC for the front and rear wheels is obtained. The proposed two-stage framework leverages the strengths of EHKF and AUKF to address different challenges in the estimation process. EHKF ensures robust force estimation under unknown noise conditions, while AUKF refines TRFC estimation by adapting to time-varying noise and system non-linearities, creating a complementary and effective approach.

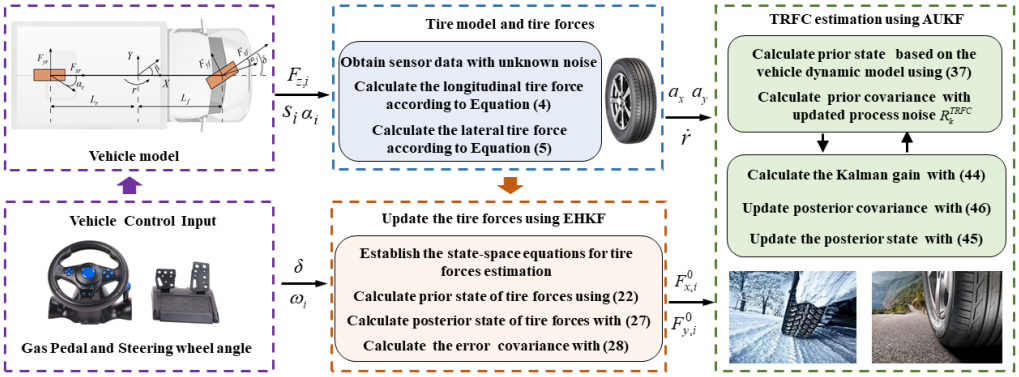

Fig. 1. Two-stage estimation scheme.

The estimation of the TRFC requires precise vehicle and tire models to be established. Taking into account the computational cost and model complexity, a single-track vehicle model is chosen to describe the vehicle's dynamic response. Furthermore, the tire forces are derived using the Dugoff tire model.

2.1. The Vehicle Model

A single-track vehicle model [33] is employed, as shown in Fig. 2. Air resistance and suspension system effects are ignored. The model assumes that the mechanical characteristics of the left and right tires are identical and can be linearly superimposed, represented by a single tire, thereby reducing the four-wheel vehicle model to a two-wheel model. Additionally, it assumes small steering angles, neglects the vehicle's roll and pitch motions, and ignores aerodynamic forces such as drag and lift. Moreover, the vehicle's centre of gravity is assumed to be positioned at the origin of the coordinate system. Unlike traditional passenger cars, which are typically front-wheel driven, heavy-duty vehicles are usually rear-wheel driven.

$$a_x = \frac{\left(F_{xf}\sin\delta + F_{xr}\right)}{m}, \tag{1}$$

$$a_y = \frac{\left(F_{yf}\cos\delta + F_{yr}\right)}{m}, \tag{2}$$

$$\dot{r}I_z = L_f\left(F_{xf}\sin\delta + F_{yf}\cos\delta\right) - L_r F_{yr}, \tag{3}$$

where β, v_x, v_y denote the sideslip angle, longitudinal vehicle velocity, and lateral vehicle velocity, a_x and a_y denote longitudinal acceleration and lateral acceleration, I_z is the inertia moment about the vehicle vertical axis, the parameters L_f and L_r denote the distance from the centre of gravity to the front axle and rear axle, m is the vehicle mass, δ is the front wheel angle, F_{xf}, F_{yf} are longitudinal and lateral forces of the front axle, F_{xr}, F_{yr} are longitudinal and lateral forces of the rear axle, r is the yaw rate. Here, we assume that the axial forces for both the front and rear axles are equal to the sum of the forces on the two front wheels and the two rear wheels, respectively.

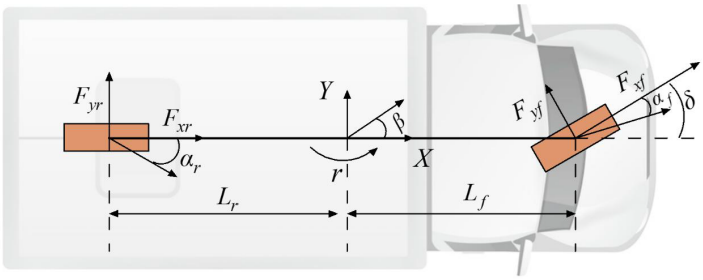

Fig. 2. Single-track vehicle model.

2.2. The Tire Model

The relationship between tire motion and forces is defined by the Dugoff tire model [34]. The corresponding equations are presented below.

$$F_{x,i} = \mu_i F_{x,i}^0 = \mu_i F_{z,i} C_{x,i} \left(\frac{s_i}{1+s_i} \right) f(L), \tag{4}$$

$$F_{y,i} = \mu_i F_{y,i}^0 = \mu_i F_{z,i} C_{y,i} \left(\frac{\tan \alpha_i}{1+s_i} \right) f(L), \tag{5}$$

$$f(L) = \begin{cases} L(2-L), & L < 1 \\ 1, & L \geq 1 \end{cases}, \tag{6}$$

$$L = \frac{1-s_i}{2\sqrt{C_x^2 s_i^2 + C_y^2 (\tan \alpha_i)^2}}, \tag{7}$$

$$F_{z,1} = \frac{mgL_r}{2(L_f+L_r)} - \frac{ma_x h}{2(L_f+L_r)} - \frac{ma_y h}{T_f} \cdot \frac{L_r}{L_f+L_r}, \tag{8}$$

$$F_{z,2} = \frac{mgL_r}{2(L_f+L_r)} - \frac{ma_x h}{2(L_f+L_r)} + \frac{ma_y h}{T_f} \cdot \frac{L_r}{L_f+L_r}, \tag{9}$$

$$F_{z,3} = \frac{mgL_f}{2(L_f+L_r)} + \frac{ma_x h}{2(L_f+L_r)} - \frac{ma_y h}{T_r} \cdot \frac{L_f}{L_f+L_r}, \tag{10}$$

$$F_{z,4} = \frac{mgL_f}{2(L_f+L_r)} + \frac{ma_x h}{2(L_f+L_r)} + \frac{ma_y h}{T_r} \cdot \frac{L_f}{L_f+L_r}, \tag{11}$$

$$s_i = \operatorname{sgn}(v_x - R\omega_i) \frac{|v_x - R\omega_i|}{\max(R\omega_i, v_x)}, \tag{12}$$

$$\alpha_1 = \delta - \arctan\left(\frac{v_y + L_f r}{v_x - \frac{T_f r}{2}}\right), \tag{13}$$

$$\alpha_2 = \delta - \arctan\left(\frac{v_y + L_f r}{v_x + \frac{T_f r}{2}}\right), \tag{14}$$

$$\alpha_3 = -\arctan\left(\frac{v_y - L_r r}{v_x - \frac{T_r r}{2}}\right), \tag{15}$$

$$\alpha_4 = -\arctan\left(\frac{v_y - L_r r}{v_x + \frac{T_r r}{2}}\right), \tag{16}$$

where μ is the TRFC, h represents the height of the centre of gravity, s_i, α_i denote the longitudinal slip ratio, wheel sideslip angle, $C_{x,i}, C_{y,i}, F_{z,i}$ represent longitudinal and lateral stiffness coefficients of tires along with vertical tire forces, $F^0_{x,i}$, $F^0_{y,i}$ are the normalized longitudinal and lateral forces, $i = 1, 2, 3, 4$, which corresponds to the left-front, right-front, left-rear, and right-rear wheels, respectively, ω_i is the wheel rotational speed, R_i is the wheel radius, T_f and T_r represent front track width and rear track width.

2.3. The EHKF

Unlike the traditional EKF, the EHKF eliminates the need for prior assumptions about noise characteristics. By minimizing the maximum estimation error, the HEKF offers greater robustness compared to the EKF. The nonlinear system model is described as follows.

$$\begin{aligned} &\begin{cases} x_{k+1} = f(x_k, u_k) + w_k \\ z_{k+1} = h(x_{k+1}, u_{k+1}) + v_{k+1} \end{cases}, \\ &x = \left[F^0_{x,i}, F^0_{y,i}\right]^T, \quad i = 1, 2, 3, 4, \end{aligned} \tag{17}$$

where $f(\cdot)$ denotes state transition function, w process noise, and v measurement noise, z is the measurement vector, $h(\cdot)$ denotes measurement transition function, u is the input vector, x represents the state vector. While $f(\cdot)$ and $h(\cdot)$ are not directly applied in the EKF update step, their Jacobian forms are utilized as the transition and observation matrices, respectively.

$$F_k = \left.\frac{\partial f}{\partial x}\right|_{\hat{x}_{k-1}|k-1}, \tag{18}$$

$$H_k = \left.\frac{\partial h}{\partial x}\right|_{\hat{x}_k|k-1}. \tag{19}$$

The EHKF not only limits the upper limit of the estimation error but also minimizes this upper limit. Thus, the cost function is defined as follows.

$$J = \frac{\sum_{k=1}^{N} \|x_k - \hat{x}_k\|^2}{\|x_0 - \hat{x}_0\|^2_{P_0^{-1}} + \sum_{k=1}^{N} \left(\|w_k\|^2_{Q_k^{-1}} + \|v_k\|^2_{R_k^{-1}} \right)}, \tag{20}$$

where x_0 is the initial state vector x_k, Q_k is the covariance matrix of the process noise, R_k is the covariance matrix of the measurement noise, and P_0 is the initial value of the state covariance matrix P_k.

The objective of establishing this loss function is to find an appropriate x_k that minimizes J. However, in real-world applications, finding the optimal solution is difficult, and suboptimal solutions are commonly used. Thus, the cost function takes the following form:

$$\text{Sup}\left\{\mathbf{x}_0, \mathbf{v}_k, \mathbf{w}_k\right\} = \frac{\sum_{k=1}^{N} \|x_k - \hat{x}_k\|^2}{\|x_0 - \hat{x}_0\|^2_{P_0^{-1}} + \sum_{k=1}^{N} \left(\|w_k\|^2_{Q_k^{-1}} + \|v_k\|^2_{R_k^{-1}} \right)} \leq \gamma^2, \tag{21}$$

where $\gamma > 0$ and γ^2 denote the thresholds that limit the upper limit of the energy of the cost function. The smaller the value of γ, the more robust the estimator becomes. Thus, the overall iterative process of constructing the EHKF is as shown below.

Time Update:

The prior state prediction

$$x_{k|k-1} = F_k x_{k-1|k-1}. \tag{22}$$

The error covariance prediction

$$P_{k|k-1} = F_k P_{k-1|k-1} F_k^T + Q_{k-1}. \tag{23}$$

Measurement Update

$$\overline{S}_k = L_k^T \overline{S}_k L_k. \tag{24}$$

$$M_k = I - \gamma \overline{S}_k P_{k|k-1} + H_k^T R_k^{-1} H_k P_{k|k-1}. \tag{25}$$

Compute the Kalman Gain

$$K_k = P_{k|k} M_k H_k^T R_k^{-1}. \tag{26}$$

Update the posterior state:

$$x_{k|k} = x_{k|k-1} + K_k \left(z_k - H_k x_{k|k-1} \right). \tag{27}$$

Update the error Covariance

$$P_{k|k} = P_{k|k-1} M_k, \tag{28}$$

Above, S_k is the state weightage matrix and L_k is the identify matrix. Further, the existence of EHKF needs to satisfy the following equation [35]:

$$P_{k|k}^{-1} + H_k^T R_k^{-1} H_k - \gamma^{-2} L_k^T L_k > 0. \tag{29}$$

For the filtering of tire forces, at this point, the Jacobi matrices F_k and H_k are both unit matrices and the matrix dimension is 8.

2.4. The AUKF

The TRFC can be treated as constant during brief time intervals. By leveraging the relationships between $F_{x,i}^0$, $F_{x,i}$, $F_{y,i}^0$ and $F_{y,i}$ as defined in Eqs. (4–5), the discrete mathematical model can be obtained through equations (1–3):

$$\begin{cases} x_{k+1}^{\mathrm{TRFC}} = f(x_k^{\mathrm{TRFC}}, u_k) + w_k^{\mathrm{TRFC}} \\ z_{k+1}^{\mathrm{TRFC}} = h(x_{k+1}^{\mathrm{TRFC}}, u_{k+1}) + v_{k+1}^{\mathrm{TRFC}} \end{cases}, \tag{30}$$

$$x^{\mathrm{TRFC}} = [\mu_1, \mu_2, \mu_3, \mu_4]^T, \quad x_{\tau+1}^{\mathrm{TRFC}} = [a_x, a_y, \dot{r}]^T. \tag{31}$$

We use the AUKF to estimate the average TRFC $\mu_f = 0.5\,(\mu_1 + \mu_2)$ for the front-wheel and the average TRFC $\mu_r = 0.5\,(\mu_3 + \mu_4)$ for the rear-wheel. The detailed iterative steps are outlined as follows:

1) Initialization:

The initial mean of x^{TRFC} and its *covariance matrix* (CM) P^{TRFC}

$$\hat{x}_0^{\mathrm{TRFC}} = E\left(x_0^{\mathrm{TRFC}}\right), \tag{32}$$

$$P_0^{\mathrm{TRFC}} = E\left[\left(x_0^{\mathrm{TRFC}} - \hat{x}_0^{\mathrm{TRFC}}\right)\left(x_0^{\mathrm{TRFC}} - \hat{x}_0^{\mathrm{TRFC}}\right)^T\right]. \tag{33}$$

2) Time steps:

The *sigma sampling points* (SSP) λ_{k-1}^i and weight ϕ_c^i, ϕ_m^i are given by

$$\begin{cases} \lambda_{k-1}^0 = \hat{x}_{k-1}^{\mathrm{TRFC}} \\ \lambda_{k-1}^i = \hat{x}_{k-1}^{\mathrm{TRFC}} + \sqrt{n+\lambda}\left(\sqrt{P_{k-1}^{\mathrm{TRFC}}}\right)_i, \quad i = 1, 2, \cdots n \\ \lambda_{k-1}^i = \hat{x}_{k-1}^{\mathrm{TRFC}} - \sqrt{n+\lambda}\left(\sqrt{P_{k-1}^{\mathrm{TRFC}}}\right)_i, \quad i = n+1, \cdots 2n \end{cases}, \tag{34}$$

$$\begin{cases} \phi_m^0 = \lambda/(n+\lambda)\,, \phi_c^0 = \lambda/(n+\lambda) + 1 + \beta - \alpha^2 \\ \phi_m^i = \phi_c^i = \lambda/(2\,(n+\lambda))\,, \quad i = 1, 2, \cdots 2n \end{cases}, \\ \begin{cases} \phi_m^0 = \lambda/(n+\lambda)\,, \phi_c^0 = \lambda/(n+\lambda) + 1 + \beta - \alpha^2 \\ \phi_m^i = \phi_c^i = \lambda/(2\,(n+\lambda))\,, \quad i = 1, 2, \cdots 2n \end{cases}, \tag{35}$$

where n is the dimension of x, λ, β, and α can be seen in [36].

The propagated SSP are updated by

$$\lambda_{k/k-1}^{*(i)} = f\left(\lambda_{k-1}^{(i)}, u_{k-1}\right). \tag{36}$$

The prior state $\hat{x}_{k/k-1}^{\mathrm{TRFC}}$ and corresponding state CM $P_{k/k-1}^{\mathrm{TRFC}}$ are calculated utilizing (37) and (38), respectively.

$$\hat{x}_{k/k-1}^{\mathrm{TRFC}} = \sum_{i=0}^{2n} \phi_m^i \lambda_{k/k-1}^{*(i)}, \tag{37}$$

$$P_{k/k-1}^{\mathrm{TRFC}} = \sum_{i=0}^{2n} \phi_c^i \left(\lambda_{k/k-1}^{*(i)} - \hat{x}_{k/k-1}^{\mathrm{TRFC}}\right)\left(\lambda_{k/k-1}^{*(i)} - \hat{x}_{k/k-1}^{\mathrm{TRFC}}\right)^T + Q_{k-1}^{\mathrm{TRFC}}, \tag{38}$$

where Q_{k-1}^{TRFC} is the CM of the process noise.

3) Measurement steps:
The new SSP λ_k^i are as follows:

$$\begin{cases} \lambda_k^0 = \hat{x}_{k/k-1}^{\mathrm{TRFC}} \\ \lambda_k^i = \hat{x}_{k/k-1}^{\mathrm{TRFC}} + \sqrt{n+\lambda}\left(\sqrt{P_{k/k-1}^{\mathrm{TRFC}}}\right)_i, \quad i = 1, 2, \cdots n \\ \lambda_k^i = \hat{x}_{k/k-1}^{\mathrm{TRFC}} - \sqrt{n+\lambda}\left(\sqrt{P_{k/k-1}^{\mathrm{TRFC}}}\right)_i, \quad i = n+1, \cdots 2n \end{cases}, \tag{39}$$

The propagated SSP are updated by

$$z_{k/k-1}^{*(i)} = h\left(\lambda_k^{(i)}, u_k\right). \tag{40}$$

The estimated output $\hat{z}_{k/k-1}$ and its CM$P_{z,k}$ are calculated using (41) and (42), respectively.

$$\hat{z}_{k/k-1}^{\mathrm{TRFC}} = \sum_{i=0}^{2n} \phi_m^i z_{k/k-1}^{*(i)}, \tag{41}$$

$$P_{z,k}^{\mathrm{TRFC}} = \sum_{i=0}^{2n} \phi_c^i \left(z_{k/k-1}^{*(i)} - \hat{z}_{k/k-1}^{\mathrm{TRFC}}\right)\left(z_{k/k-1}^{*(i)} - \hat{z}_{k/k-1}^{\mathrm{TRFC}}\right)^T + R_k^{\mathrm{TRFC}}, \tag{42}$$

where R_k^{TRFC} is the CM of the measurement noise.
The CM$P_{xz,k}^{\mathrm{TRFC}}$ is given by

$$P_{xz,k}^{\mathrm{TRFC}} = \sum_{i=0}^{2n} \phi_c^i \left(z_{k/k-1}^{*(i)} - \hat{x}_{k/k-1}^{\mathrm{TRFC}}\right)\left(z_{k/k-1}^{*(i)} - \hat{x}_{k/k-1}^{\mathrm{TRFC}}\right)^T. \tag{43}$$

The gain matrix K_k^{TRFC}can be calculated using (44) and the posterior state $\hat{x}_k^{\mathrm{TRFC}}$ and its CMP_k^{TRFC} are updated using (45) and (46).

$$K_k^{\mathrm{TRFC}} = P_{xz,k}^{\mathrm{TRFC}}\left(P_{z,k}^{\mathrm{TRFC}}\right)^{-1}, \tag{44}$$

$$\hat{x}_k^{\mathrm{TRFC}} = \hat{x}_{k,k/k-1}^{\mathrm{TRFC}} + K_k^{\mathrm{TRFC}}\left(z_k^{\mathrm{TRFC}} - \hat{z}_{k/k-1}^{\mathrm{TRFC}}\right), \tag{45}$$

$$P_k^{\mathrm{TRFC}} = P_{k/k-1}^{\mathrm{TRFC}} - K_k^{\mathrm{TRFC}} P_{z,k}^{\mathrm{TRFC}}\left(K_k^{\mathrm{TRFC}}\right)^T. \tag{46}$$

The above iterative process of UKF presumes that the R_k^{TRFC} is known, and in order to adapt to the variable driving conditions, the dynamic update of R_k^{TRFC} is performed as follows:

$$\varepsilon_k = z_k^{\mathrm{TRFC}} - \hat{z}_{k/k-1}^{\mathrm{TRFC}}, \tag{47}$$

$$\hat{C}_k = \frac{\sum_{i=k-L+1}^{k} \varepsilon_i \varepsilon_i^T}{L}, \tag{48}$$

$$\hat{R}_k^{\mathrm{TRFC}} = \hat{C}_k + \sum_{i=0}^{2n+1}\left[\phi_c^i\left(z_{k/k-1}^{*(i)} - \hat{z}_{k/k-1}^{\mathrm{TRFC}} + \hat{C}_k\right)\left(z_{k/k-1}^{*(i)} - \hat{z}_{k/k-1}^{\mathrm{TRFC}} + \hat{C}_k\right)^T\right]. \tag{49}$$

3. Simulation

We developed an advanced integrated simulation platform using *TRUCKSIM* and *SIMULINK* (see Fig. 3). *TRUCKSIM* is a sophisticated simulation software designed for modelling the dynamic behaviour of commercial vehicles, including trucks, buses, and trailers. It provides a highly accurate representation of vehicle handling, suspension systems, and tire characteristics, making it an invaluable tool for engineers. The software allows for the simulation of various driving scenarios, including road types, load conditions, and driver inputs, to analyse vehicle performance. One of its key advantages is the ability to test vehicle designs virtually, reducing the need for costly physical prototypes and real-world testing. *TRUCKSIM* provides a high-fidelity vehicle model that captures detailed dynamics, including suspension, tire, and steering system characteristics. The model incorporates key parameters such as vehicle mass, inertia, and braking system performance. The vehicle model parameters used in the experiment are shown in Table 1. This high level of accuracy allows for realistic simulations of vehicle behaviour in various driving conditions and scenarios. As a result, the tire forces and TRFC generated in *TRUCKSIM* can be used as *reference values* (RVs). The EHKF and AUKF are implemented in *SIMULINK*. To validate the proposed approach, random Gaussian noise was added to the sensor signals, and tests were conducted on asphalt as well as ice road surfaces. It should be noted that since a single-track model is selected, the forces shown in the result figures are those for the front and rear axles, not the individual tire forces, for the sake of consistency in validation. Additionally, the TRFC represents the average TRFC for the front and rear wheels, rather than the TRFC for a single tire.

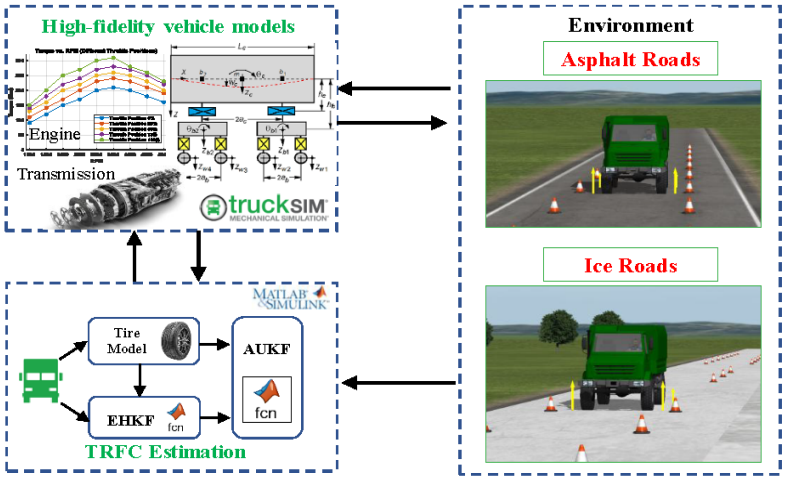

Fig. 3. Integrated simulation platform.

Table 1. Truck model parameters.

Symbol	Value	Symbol	Value
m	6900 kg	T_f	1.975 m
I_z	5757 kg · m^2	T_r	1.975 m
L_f	1.4 m	h	0.975 m
L_r	2.5 m	g	9.8 m/s^2

3.1. Tests on asphalt roads

A steering manoeuvre involving acceleration on asphalt roads is performed, with the TRFC set at 0.85. The parameters chosen for tire force estimation in the EHKF method are as follows: the measurement noise is $R = \text{diag}\,[10, 10, 10, 10, 1, 1, 1,]$, and the process noise is $Q = \text{diag}\,[1, 1, 1, 1, 1, 1, 1, 1] \cdot 0.01$. The front wheel angle and vehicle velocity are shown in Fig. 4a and Fig. 4b. From these two figures, we can see that the vehicle's initial speed is 20 km/h, after which it accelerates to nearly 70 km/h by the end of the simulation. Meanwhile, the vehicle performs lane change manoeuvres during this time.

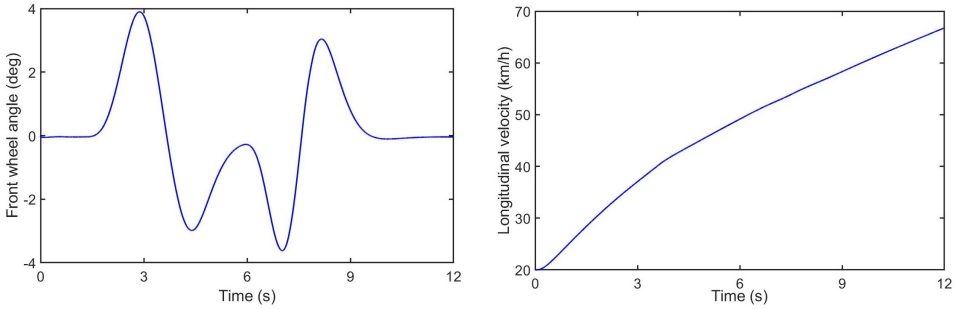

(a) (b)

Fig. 4. Vehicle state: a) front wheel angle on asphalt roads, b) vehicle speed on asphalt roads.

Figures 5a and 5b illustrate the estimated curves of longitudinal forces for the front and rear axles. Figures 5c and 5d show the estimated lateral forces for the front and rear axles. The red solid line represents the RV, while the green dashed line shows the axial forces calculated directly from the Dugoff model and the noisy sensor signals. The blue solid line represents the axial forces after filtering with the EHKF. We can observe that direct calculations using the tire model result in significant fluctuations and deviations from the RV due to severe noise interference. Since the noise is set randomly, applying the EHKF clearly shows that the filtered forces for both the front and rear axles are much closer to the RV with reduced fluctuations. Table 2 displays the *root mean square error* (RMSE) for both methods. It is evident that the RMSE for EHKF is lower than that of the direct calculation based on the tire model. This is because the EHKF can minimize the maximum error even when the statistical characteristics of the noise are unknown.

Table 2. RMSE of Different Methods on Asphalt Roads.

Symbol	Dugoff model	EHKF
F_{xf}	29.61	18.41
F_{xr}	388.52	338.70
F_{yf}	800.92	602.76
F_{yr}	1080.20	306.06

Figures 6a and 6b illustrate the TRFC estimation curves for the front and rear wheels, respectively. The red solid line represents the RV, the green solid line shows the values estimated using the UKF algorithm, and the blue solid line shows the values estimated using the AUKF algorithm. As seen in the two figures, the actual TRFC is 0.85. In Fig. 6a, the TRFC estimation curve of the front wheel only begins to rapidly approach the RV around 1.63 seconds. This is because the heavy-duty vehicle is rear-wheel drive, and even though the vehicle is accelerating,

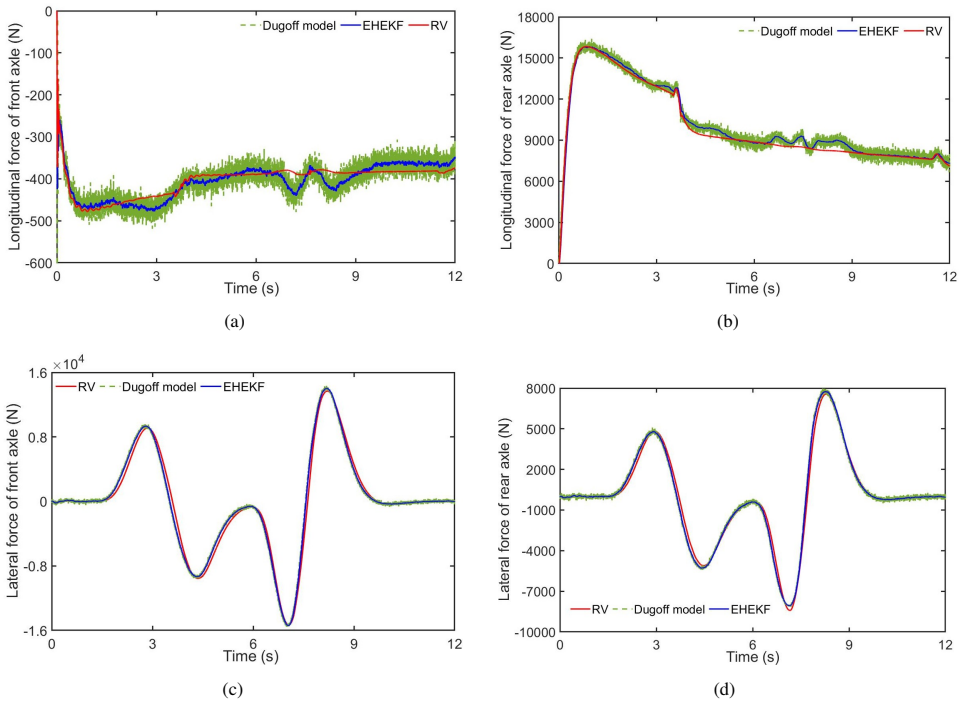

Fig. 5. Forces of the front and rear axles: a) longitudinal force of the front axle on asphalt roads, b) the longitudinal force of the rear axle on asphalt roads, c) lateral force of the front axle on asphalt roads, d) lateral force of the rear axle on asphalt roads.

the excitation on the front axle is still minimal. The rapid convergence toward the RV after 1.63 seconds occurs because steering excitation starts to increase significantly at that point. Since the noise is randomly assigned, the AUKF can dynamically adjust the noise covariance matrix R allowing it to better track the RV, while the UKF estimation curve fluctuates more and does not converge to the true value. In Fig. 6b, since the vehicle begins accelerating right away and the rear axle is the driving axle, the estimation curves from both algorithms quickly approach the RV at the start of the simulation. However, due to the lack of noise adaptability in the UKF, its estimation accuracy is lower than that of the AUKF.

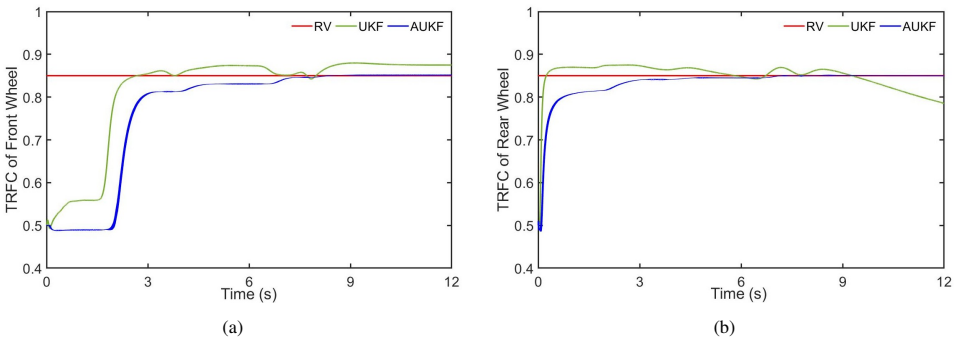

Fig. 6. TRFC: a) for the front wheel on asphalt roads, b) for the rear wheel on asphalt roads.

3.2. Test on ice roads

On icy and snowy roads, high speeds can easily lead to instability, so the vehicle speed is set to 30 km/h, and the vehicle performs a non-standard lane change manoeuvre. Figures 7a and 7b depict the changes in the front wheel steering angle and vehicle speed, respectively. The front wheel steering angle is more irregular compared to the experiment on asphalt roads, while the vehicle speed remains relatively stable at 30 km/h for constant-speed driving. The parameters for the EHKF are as follows: $Q = \text{diag}\,[1, 1, 1, 1, 1, 1, 1, 1] \cdot 0.01$, $R = \text{diag}\,[10, 10, 10, 10, 1, 1, 1,]$.

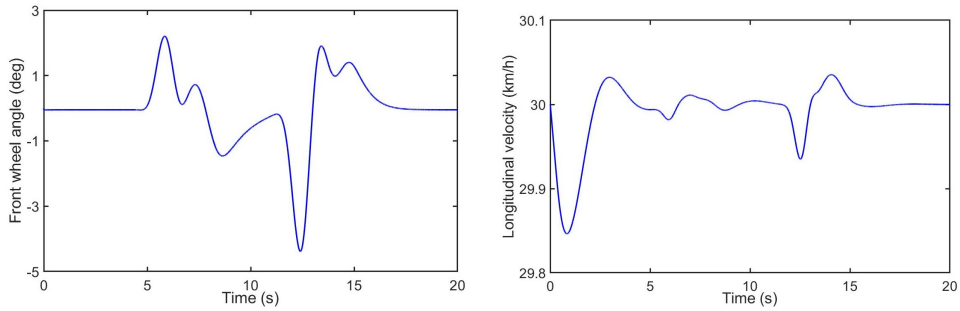

(a) (b)

Fig. 7. Vehicle state: a) front wheel angle on ice roads, b) vehicle speed on ice roads.

In Fig. 8a and Fig. 8b, the estimated longitudinal forces for both the front and rear axles are displayed. In Fig. 8c and Fig. 8d, the estimated lateral forces for the front and rear axles are shown. The influence of random noise, which was introduced into the system, is clearly visible in these graphs. The forces, when directly calculated using the tire model, exhibit considerable variations and significant deviations from the RV. These discrepancies primarily arise due to the tire model's susceptibility to noise interference, making it challenging to obtain reliable estimations under noisy conditions. When the EHKF is applied, a marked improvement in estimation precision can be observed. The filtered force estimates on both the front and rear axles align much closer with the RV, showing significantly fewer fluctuations. This demonstrates the robustness of the EHKF which proves more effective at handling noise compared to direct calculations based on the tire model. The EHKF is particularly adept at managing uncertainties even when the statistical properties of the noise remain unknown. Its capability to minimize the maximum estimation error is crucial for achieving this enhanced performance. A comparison of RMSE for both methods is presented in Table 3. It is evident that the RMSE for the EHKF is notably lower than for the direct method using the tire model. The ability of the EHKF to adapt to random noise and produce more accurate estimations, even under uncertain and dynamic conditions, underscores its superiority.

Table 3. RMSE of Different Methods on Ice Roads.

Symbol	Dugoff model	EHKF
F_{xf}	88.90	45.58
F_{xr}	318.80	171.54
F_{yf}	2797.50	2420.70
F_{yr}	1745.30	845.08

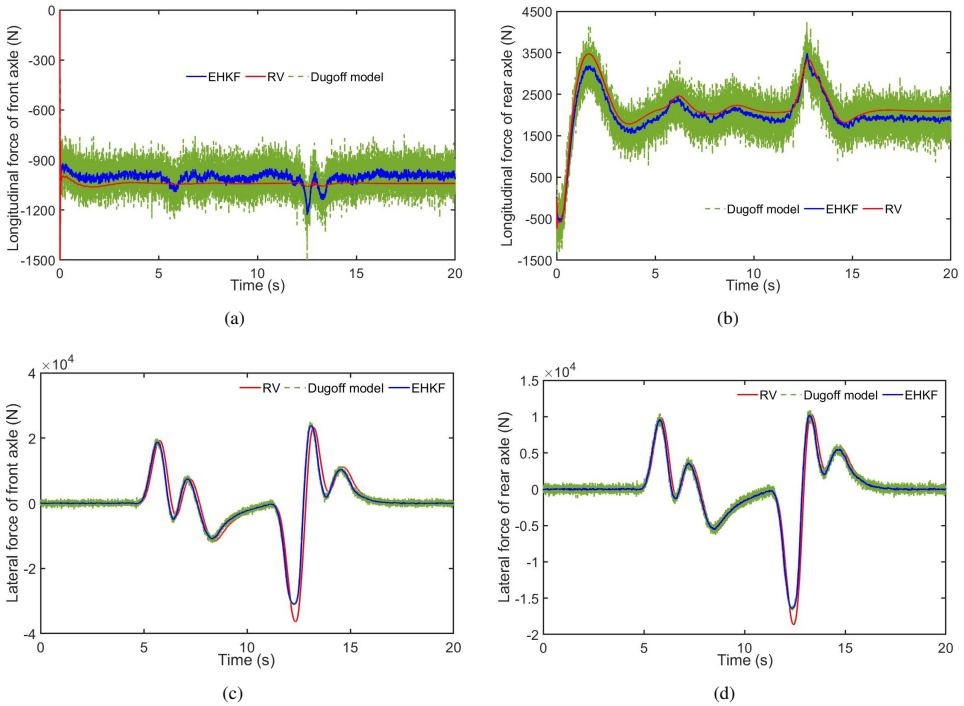

Fig. 8. Forces for the front and rear axles: a) longitudinal force of the front axle on ice roads, b) the longitudinal force of the rear axle on ice roads, c) lateral force of the front axle on ice roads, d) lateral force of the rear axle on ice roads.

The TRFC estimation curves for the front and rear wheels are illustrated in Fig. 9a and Fig. 9b, respectively. Similar to the first experimental scenario, the TRFC of the front wheels only rapidly approaches the RV after more than 5 seconds, while the TRFC for the rear wheels quickly converges to the RV from the start. The reason for this behaviour is the same as in the asphalt road experiment. Likewise, from both figures, we can see that the AUKF curves eventually converge to the RV, whereas the UKF, lacking the ability to dynamically adapt to measurement noise, exhibits greater fluctuations and fails to track the RV. Through the two experiments mentioned above, we can observe that the proposed estimation scheme demonstrates adaptability to different noise interferences and is capable of identifying the TRFC across various road surfaces.

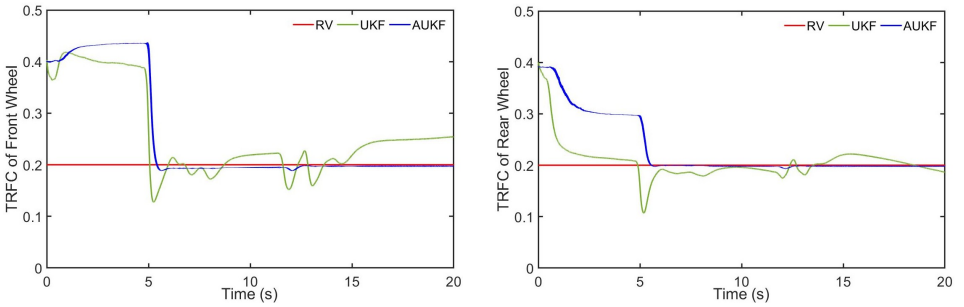

Fig. 9. TRFC: a) of the front wheel on ice roads, b) of the rear wheel on ice roads.

4. Conclusion

In this work, a two-stage adaptive identification framework is proposed that combines EHKF and AUKF, enabling accurate TRFC estimation under unknown and time-varying measurement noise conditions. Initially, in the cases where the statistical characteristics of noise are unknown, the EHKF combined with the tire model provides precise force estimations for both the front and rear axles. Subsequently, considering the time-varying nature of noise, the AUKF, together with the vehicle model and axial force data, is utilized to estimate the TRFC for the front and rear wheels. Simulation tests conducted for various road surfaces demonstrate that the two-stage adaptive identification scheme outperforms the unscented Kalman filter in terms of both accuracy and stability.

Since it is assumed that the model parameters are constant and known in advance during the estimation process, there is an opportunity to further improve the robustness and flexibility of the proposed framework. In the future, we aim to integrate parameter identification methods into the estimation framework to address potential variations in model parameters. This integration will allow the system to adapt more effectively to dynamic conditions, thereby enhancing the algorithm's overall performance and making it more applicable to real-world scenarios where exact parameter knowledge may not always be available. Furthermore, while some experimental sites and equipment are currently unavailable, plans are in place to conduct real-vehicle experiments as soon as the required resources are accessible. These real-world tests will be essential to validate the practicality and robustness of the proposed algorithm under actual operating conditions, ensuring its applicability in diverse vehicle environments and road conditions.

Acknowledgements

This work was supported by the National Natural Science Funds for under Grant 52402482, in part sponsored by the QingLan Project of Jiangsu Higher Education Institutions (JSQL2022 and 2023), and in part by R&D Projects from Industry under Grant P0046083, P0048792.

References

[1] Zhou, C., Yu, L., Li, Y., Lu, Z., & Song, J. (2022). A layered roll stability control strategy for commercial vehicles based on adaptive model predictive control. *Vehicle System Dynamics*, *61*(12), 3067–3088. https://doi.org/10.1080/00423114.2022.2154229

[2] Wang, P., Zhang, X., Shi, J., Gou, B., Zhang, L., Chen, H., & Hu, Y. (2023). Rollover prevention control of electric vehicles based on Multi-Objective Optimization coordination under extreme conditions. *IEEE Transactions on Vehicular Technology*, *72*(10), 12784–12798. https://doi.org/10.1109/tvt.2023.3274591

[3] Yang, X., Wu, C., He, Y., Lu, X., & Chen, T. (2022). A Dynamic Rollover Prediction Index of Heavy-Duty Vehicles with a Real-Time Parameter Estimation Algorithm Using NLMS method. *IEEE Transactions on Vehicular Technology*, *71*(3), 2734–2748. https://doi.org/10.1109/tvt.2022.3144629

[4] Pietruch, M., Wetula, A., & Młyniec, A. (2022). Verification of hardware-in-the-loop test bench for evaluating steering wheel angle sensor performance for steer-by-wire system. *Metrology and Measurement Systems*. https://doi.org/10.24425/mms.2022.143065

[5] Wang, Y., Yin, G., Li, Y., Ullah, S., Zhuang, W., Wang, J., Zhang, N., & Geng, K. (2019). Self-learning control for coordinated collision avoidance of automated vehicles. *Proceedings of the Institution of Mechanical Engineers Part D Journal of Automobile Engineering*, *235*(4), 1149–1163. https://doi.org/10.1177/0954407019887884

[6] Wang, Y., Chen, H., Yin, G., Mo, Y., De Boer, N., & Lv, C. (2024). Motion state estimation of preceding vehicles with packet loss and unknown model parameters. *IEEE/ASME Transactions on Mechatronics*, *29*(5), 3461–3472. https://doi.org/10.1109/tmech.2023.3345956

[7] Cheng, S., Li, L., Guo, H., Chen, Z., & Song, P. (2019). Longitudinal Collision Avoidance and Lateral Stability Adaptive control system based on MPC of autonomous vehicles. *IEEE Transactions on Intelligent Transportation Systems*, *21*(6), 2376–2385. https://doi.org/10.1109/tits.2019.2918176

[8] Wang, Y., Yin, G., Hang, P., Zhao, J., Lin, Y., & Huang, C. (2024). Fundamental estimation for tire road friction coefficient: a model-based learning framework. *IEEE Transactions on Vehicular Technology*, 1–12. https://doi.org/10.1109/tvt.2024.3464524

[9] Khaleghian, S., Emami, A., & Taheri, S. (2017). A technical survey on tire-road friction estimation. *Friction*, *5* (2), 123–146. https://doi.org/10.1007/s40544-017-0151-0

[10] Tuononen, A. (2008). Optical position detection to measure tyre carcass deflections. *Vehicle System Dynamics*, *46* (6), 471–481. https://doi.org/10.1080/00423110701485043

[11] Erdogan, G., Alexander, L., & Rajamani, R. (2010). Estimation of tire-road friction coefficient using a novel wireless piezoelectric tire sensor. *IEEE Sensors Journal*, *11* (2), 267–279. https://doi.org/10.1109/jsen.2010.2053198

[12] Xu, N., Askari, H., Huang, Y., Zhou, J., & Khajepour, A. (2020). Tire force estimation in intelligent tires using machine learning. *IEEE Transactions on Intelligent Transportation Systems*, *23*(4), 3565–3574. https://doi.org/10.1109/tits.2020.3038155

[13] Kim, H., Han, J., Lee, S., Kwag, J., Kuk, M., Han, I., & Kim, M. (2020). A Road Condition Classification Algorithm for a Tire Acceleration Sensor using an Artificial Neural Network. *Electronics*, *9*(3), 404. https://doi.org/10.3390/electronics9030404

[14] Leng, B., Jin, D., Xiong, L., Yang, X., & Yu, Z. (2020). Estimation of tire-road peak adhesion coefficient for intelligent electric vehicles based on camera and tire dynamics information fusion. *Mechanical Systems and Signal Processing*, *150*, 107275. https://doi.org/10.1016/j.ymssp.2020.107275

[15] Yu, M., Xu, X., Wu, C., Li, S., Li, M., & Chen, H. (2021). Research on the prediction model of the friction coefficient of asphalt pavement based on tire-pavement coupling. *Advances in Materials Science and Engineering*, *2021*(1). https://doi.org/10.1155/2021/6650525

[16] Guo, H., Yin, Z., Cao, D., Chen, H., & Lv, C. (2018). A review of Estimation for Vehicle Tire-Road Interactions toward Automated Driving. *IEEE Transactions on Systems Man and Cybernetics Systems*, *49*(1), 14–30. https://doi.org/10.1109/tsmc.2018.2819500

[17] Wang, Y., Hu, J., Wang, F., Dong, H., Yan, Y., Ren, Y., Zhou, C., & Yin, G. (2022). Tire Road friction Coefficient Estimation: Review and Research Perspectives. *Chinese Journal of Mechanical Engineering*, *35*(1). https://doi.org/10.1186/s10033-021-00675-z

[18] Lee, C., Hedrick, K., & Yi, K. (2004). Real-time slip-based estimation of maximum tire-road friction coefficient. *IEEE/ASME Transactions on Mechatronics*, *9*(2), 454–458. https://doi.org/10.1109/tmech.2004.828622

[19] Cui, G., Dou, J., Li, S., Zhao, X., Lu, X., & Yu, Z. (2017). Slip control of electric vehicle based on tire-road friction coefficient estimation. *Mathematical Problems in Engineering*, *2017*(1). https://doi.org/10.1155/2017/3035124

[20] Sharifzadeh, M., Senatore, A., Farnam, A., Akbari, A., & Timpone, F. (2018). A real-time approach to robust identification of tyre-road friction characteristics on mixed-μ roads. *Vehicle System Dynamics*, *57*(9), 1338–1362. https://doi.org/10.1080/00423114.2018.1504974

[21] Zhao, Y., Li, H., Lin, F., Wang, J., & Ji, X. (2017). Estimation of road friction coefficient in different road conditions based on vehicle braking dynamics. *Chinese Journal of Mechanical Engineering*, *30*(4), 982–990. https://doi.org/10.1007/s10033-017-0143-z

[22] Enisz, K., Szalay, I., Kohlrusz, G., & Fodor, D. (2014). Tyre-road friction coefficient estimation based on the discrete-time extended Kalman filter. *Proceedings of the Institution of Mechanical Engineers Part D Journal of Automobile Engineering*, *229*(9), 1158–1168. https://doi.org/10.1177/0954407014556115

[23] Castillo, J.J., Cabrera, J.A., Guerra, A.J., & Simón, A. (2015). A novel electrohydraulic brake system with tire-road friction estimation and continuous brake pressure control. *IEEE Transactions on Industrial Electronics*, *63*(3), 1863–1875. https://doi.org/10.1109/tie.2015.2494041

[24] Paul, D., Velenis, E., Cao, D., & Dobo, T. (2016). Optimal μ-Estimation-based Regenerative Braking Strategy for an AWD HEV. *IEEE Transactions on Transportation Electrification*, *3*(1), 249–258. https://doi.org/10.1109/tte.2016.2603010

[25] Hu, J., Rakheja, S., & Zhang, Y. (2020). Real-time estimation of tire-road friction coefficient based on lateral vehicle dynamics. *Proceedings of the Institution of Mechanical Engineers Part D Journal of Automobile Engineering*, *234*(10–11), 2444–2457. https://doi.org/10.1177/0954407020929233

[26] Ren, H., Chen, S., Shim, T., & Wu, Z. (2014). Effective assessment of tyre-road friction coefficient using a hybrid estimator. *Vehicle System Dynamics*, *52*(8), 1047–1065. https://doi.org/10.1080/00423114.2014.918629

[27] Wang, Y., Lv, C., Yan, Y., Peng, P., Wang, F., Xu, L., & Yin, G. (2021). An integrated scheme for coefficient estimation of tire-road friction with mass parameter mismatch under complex driving scenarios. *IEEE Transactions on Industrial Electronics*, *69*(12), 13337–13347. https://doi.org/10.1109/tie.2021.3134072

[28] Wang, Y., Zhang, Z., Wei, H., Yin, G., Huang, H., Li, B., & Huang, C. (2023). A novel fault-tolerant scheme for multi-model ensemble estimation of tire road friction coefficient with missing measurements. *IEEE Transactions on Intelligent Vehicles*, *9*(1), 1066–1078. https://doi.org/10.1109/tiv.2023.3336048

[29] McBride, S., Sandu, C., Alatorre, A., & Victorino, A. (2018). Estimation of Vehicle Tire-Road Contact Forces: A Comparison between Artificial Neural Network and Observed Theory Approaches. *SAE Technical Papers on CD-ROM/SAE Technical Paper Series*. https://doi.org/10.4271/2018-01-0562

[30] Xu, N., Askari, H., Huang, Y., Zhou, J., & Khajepour, A. (2020b). Tire force estimation in intelligent tires using machine learning. *IEEE Transactions on Intelligent Transportation Systems*, *23*(4), 3565–3574. https://doi.org/10.1109/tits.2020.3038155

[31] Sadeghi, S.M., Mashadi, B., Amirkhani, A., & Salari, A.H. (2022). Maximum tire/road friction coefficient prediction based on vehicle vertical accelerations using wavelet transform and neural network. *Journal of the Brazilian Society of Mechanical Sciences and Engineering*, *44*(8). https://doi.org/10.1007/s40430-022-03631-7

[32] Chen, L., Qin, Z., Hu, M., Bian, Y., Peng, X., & Pan, W. (2024). Data-enabled tire-road friction estimation based on explainable dynamics mechanism under straight stationary driving maneuvers. *IEEE Transactions on Intelligent Transportation Systems*, *25*(6), 5854–5866. https://doi.org/10.1109/tits.2023.3339333

[33] Badji, B., Fenaux, E., Bagdouri, M.E., & Miraoui, A. (2008). Nonlinear single track model analysis using Volterra series approach. *Vehicle System Dynamics*, *47*(1), 81–98. https://doi.org/10.1080/00423110801910957

[34] Wang, Y., Yin, G., Hang, P., Zhao, J., Lin, Y., & Huang, C. (2024b). Fundamental estimation for tire road friction coefficient: a model-based learning framework. *IEEE Transactions on Vehicular Technology*, 1–12. https://doi.org/10.1109/tvt.2024.3464524

[35] Hassibi, B., Sayed, A., & Kailath, T. (1996). Linear estimation in Krein spaces. II. Applications. *IEEE Transactions on Automatic Control*, *41*(1), 34–49. https://doi.org/10.1109/9.481606

[36] Zhang, G., Luo, J., Xu, H., Wang, Y., Wang, T., Lin, J., & Liu, Y. (2022). An improved UKF algorithm for extracting weak signals based on RBF neural network. *IEEE Transactions on Instrumentation and Measurement*, *71*, 1–14. https://doi.org/10.1109/tim.2022.3192868

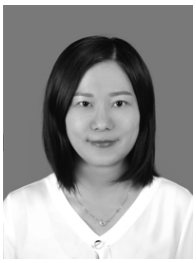

Fengjiao Zhang received the Ph.D. degree in vehicle engineering from Nanjing University of Aeronautics and Astronautics, Nanjing, China, in 2017. She is currently an Associate Professor with the School of Vehicle Engineering, Changzhou Vocational Institute of Mechatronic Technology, Changzhou, China. She was once a Visiting Scholar at Mechanical Engineering, Southeast University. She is also currently a training target for young and middle-aged academic leaders of Qinglan Project in Jiangsu Province. Her research interests include vehicle state and parameter estimation, as well as active safety control of automobiles.

Ting Meng received the B.Sc. degree in traffic and transportation in 2014 from Liaocheng University, Liaocheng, China. Now he is currently studying toward the M.S. degree in Electric Vehicles at the Hong Kong Polytechnic University. He is also a reviewer for multiple SCI journals and academic conferences. His current research interests include active vehicle safety control, vehicular networks, collision avoidance control, *etc.*

Bo Zhang received the Ph.D. degree in School of Materials Science and Engineering, Shanghai Jiao Tong University, Shanghai, China, in 2009. He is currently a Professor with the School of Vehicle Engineering, Changzhou Vocational Institute of Mechatronic Technology, Changzhou, China. He is also currently a national-level teaching master and leader of the teaching innovation team. His research interests include vehicle dynamics and automotive active safety control.

Yan Wang received the Ph.D. degree in mechanical engineering from Southeast University, Nanjing, China, in 2022. He was a research fellow with Nanyang Technological University. He is currently a research associate with The Hong Kong Polytechnical University. His current research interests include vehicle system dynamics and automotive active safety control, where he has contributed to over 50 papers and obtained over 10 patents. Dr. Wang serves as an Associate Editor for the Metrology and Measurement Systems, an Editorial board member for Measurement Science Review, and a Youth Editorial board member for the Chinese Journal of Mechanical Engineering. He was the recipient of the Outstanding Paper of China Mechanical Engineering in 2019, the Outstanding Reviewer of the Chinese Journal of Mechanical Engineering in 2022 and 2023.

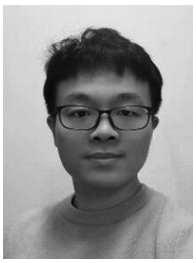

Lanchun Zhang received the Ph.D. degree in the School of Mechanical Engineering, Nanjing University of Science and Technology, Nanjing, China, in 2009. He is currently a Professor with the School of Vehicle and Jiao Tong Engineering, Jiangsu University of Technology, Chang Zhou China. He is also currently a third-level training target "333 Talent Project" and a high-level talent training target of Six Talent Peak in Jiangsu Province. His research interests include Control and Optimization of Transmission Systems for New Energy Vehicles.